Article

Superheating gold beyond the predicted entropy catastrophe threshold

https://doi.org/10.1038/s41586-025-09253-y

Received: 26 November 2024

Accepted: 6 June 2025

Published online: 23 July 2025

Open access

Check for updates

Thomas G. White[1]✉, Travis D. Griffin[1], Daniel Haden[1], Hae Ja Lee[2], Eric Galtier[2], Eric Cunningham[2], Dimitri Khaghani[2], Adrien Descamps[2,3], Lennart Wollenweber[4], Ben Armentrout[2], Carson Convery[2,5], Karen Appel[4], Luke B. Fletcher[2], Sebastian Goede[4], J. B. Hastings[2], Jeremy Iratcabal[1], Emma E. McBride[2,3], Jacob Molina[1,6,7], Giulio Monaco[8], Landon Morrison[1,9], Hunter Stramel[1], Sameen Yunus[2,10], Ulf Zastrau[4], Siegfried H. Glenzer[2], Gianluca Gregori[9], Dirk O. Gericke[11] & Bob Nagler[2]

In their landmark study[1], Fecht and Johnson unveiled a phenomenon that they termed the 'entropy catastrophe', a critical point where the entropy of superheated crystals equates to that of their liquid counterparts. This point marks the uppermost stability boundary for solids at temperatures typically around three times their melting point. Despite the theoretical prediction of this ultimate stability threshold, its practical exploration has been prevented by numerous intermediate destabilizing events, colloquially known as a hierarchy of catastrophes[2–5], which occur at far lower temperatures. Here we experimentally test this limit under ultrafast heating conditions, directly tracking the lattice temperature by using high-resolution inelastic X-ray scattering. Our gold samples are heated to temperatures over 14 times their melting point while retaining their crystalline structure, far surpassing the predicted threshold and suggesting a substantially higher or potentially no limit for superheating. We point to the inability of our samples to expand on these very short timescales as an important difference from previous estimates. These observations provide insights into the dynamics of melting under extreme conditions.

The development of short-pulse lasers has been instrumental in bypassing the intermediate destabilizing events that occur during superheating and has allowed experiments to approach the entropy catastrophe threshold[4–6]. Experiments using heating rates exceeding 10^{14} K s^{-1} have achieved superheating within the range of $T \approx 1.4T_m - 2.1T_m$, where T_m is the melting temperature, nearing but not fully reaching the anticipated limit[7–11]. Notwithstanding the advancements in heating rates, a direct, model-independent method for accurately measuring ion temperatures in hot, solid-density systems has remained elusive, which constitutes a major roadblock to drawing precise and reliable conclusions about superheating. Indeed, earlier methodologies often relied on indirect measures of ion temperature through analysis of material structure or energy absorption[12]. In response to this challenge, we utilize inelastic X-ray scattering in the backscattering regime to directly ascertain ion velocity distributions and thus determine the ion temperatures.

Leveraging this pioneering technique, we show that gold subjected to short-pulse laser irradiation unambiguously reaches heating rates exceeding 10^{15} K s^{-1}, propelling the ions to temperatures of $T \approx 14T_m$ without losing the solid structure. This measurement not only surpasses the previously predicted bounds of the entropy catastrophe but also suggests a much higher threshold for the superheating of solids, thereby rewriting the fundamental understanding of the stability of the solid phase under extreme conditions.

Measuring the lattice temperature

We use high-resolution inelastic X-ray scattering to accurately measure ion temperatures in gold samples subjected to intense laser heating. Under these conditions, photons scattering off the ions experience an energy shift similar to a Doppler shift, enabling us to determine the velocity distribution and, consequently, the temperature from the resulting spectral broadening of the incident X-rays.

Scattering from phonon modes in crystals is a well-established technique that, in polycrystals, provides information on the phonon density of states[13]. In our backscattering geometry, the spectrum transitions to a Gaussian profile, a behaviour that emerges in the multiphonon limit at high momentum transfers and temperatures well above the Debye temperature[14,15] (see Methods for details). Moreover, the phonon–phonon equilibration rate is an order of magnitude higher than the electron–phonon equilibration rate in gold, allowing us to ascribe a single temperature (T_i) to the phonon subsystem[16]. As a result, the Gaussian profile has a full-width at half-maximum (FWHM) of ΔE_{therm}, which determines the temperature from the average velocities of the ions. This relationship is given by

[1]Department of Physics, University of Nevada, Reno, NV, USA. [2]SLAC National Accelerator Laboratory, Menlo Park, CA, USA. [3]School of Mathematics and Physics, Queen's University Belfast, Belfast, UK. [4]European XFEL GmbH, Schenefeld, Germany. [5]Department of Physics, Columbia University, New York, NY, USA. [6]Department of Astrophysical Sciences, Princeton University, Princeton, NJ, USA. [7]Princeton Plasma Physics Laboratory, Princeton University, Princeton, NJ, USA. [8]Department of Physics and Astronomy "Galileo Galilei", University of Padova, Padua, Italy. [9]Department of Physics, University of Oxford, Oxford, UK. [10]Department of Physics, University of California, Merced, CA, USA. [11]Centre for Fusion, Space and Astrophysics, Department of Physics, University of Warwick, Coventry, UK. ✉e-mail: tgwhite@unr.edu

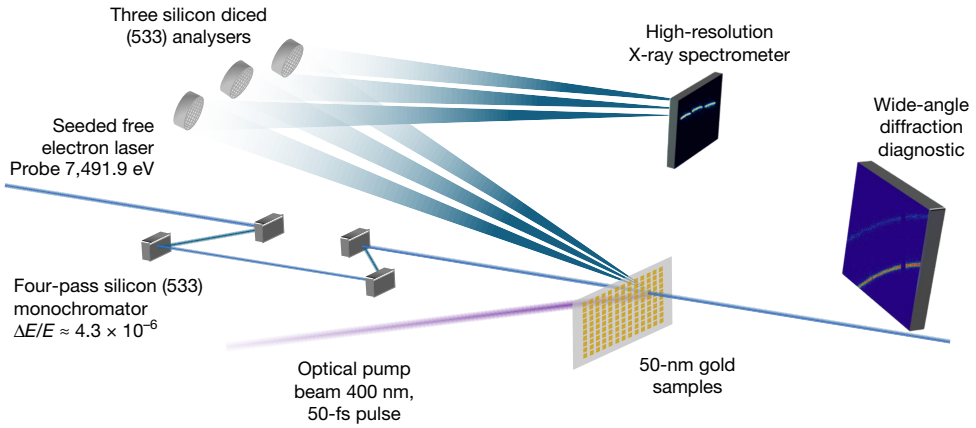

Fig. 1 | Diagram of the experimental set-up. X-rays produced by the LCLS in the seeded operation mode (E_0 = 7,491.9 eV, $\Delta E \approx 0.50$ eV) are passed through a 4-pass Si (533) monochromator, yielding a total bandwidth of about 32 meV. The X-rays are then used to probe a 50-nm-thick gold foil that is supported on a nickel grid. The primary diagnostic of the probe involves a spectrometer comprising three Si (533) diced analysers and an X-ray camera positioned to capture scattering at an angle of about 170°. A large-area detector (ePix10K) is used to measure the diffraction signal from the (111) and (200) diffraction lines of solid gold.

$$T_i = \frac{1}{k_B}\frac{1}{4}\frac{m_i c^2}{8\ln 2}\left(\frac{\Delta E_{therm}}{E_0}\right)^2, \quad (1)$$

where m_i is the mass of the ion, c is the speed of light, k_B is the Boltzmann constant and E_0 is the X-ray energy. Notably, this form matches that of a classical gas with a Maxwell–Boltzmann distribution[17,18] and is independent of the interatomic potential or the phonon density of states.

The energy shifts of the scattered photons in equation (1) are very small, with a broadening of just approximately 25 meV predicted for gold at a temperature of 1,000 K. In addition, samples are typically very short-lived when heating rates exceed 10^{15} K s^{-1}. Consequently, measuring the broadening owing to the ion motion necessitates a high-brightness X-ray source paired with a high-resolution spectrometer. Recent advances at the Matter in Extreme Conditions (MEC) instrument[19,20] at the Linac Coherent Light Source (LCLS), along with spectrometer technologies developed at the European Synchrotron Radiation Facility[21], have enabled experiments with instrument functions of about 50 meV (refs. 22–24) and an X-ray probe of 40 fs duration.

The experimental configuration is illustrated in Fig. 1. We used a 50-nm-thick polycrystalline gold sample mounted on a nickel grid irradiated by a 45-fs, 400-nm wavelength short-pulse laser from the MEC facility. The laser was focused to a spot approximately 100 µm in radius with resulting fluences of 1.9 J cm^{-2} to 4.9 J cm^{-2}. A calibrated camera outside the vacuum chamber recorded the laser fluence during each shot. The LCLS delivered an X-ray beam with a photon energy of 7,491.9 eV, monochromated by a 4-bounce channel-cut Si-533 monochromator set at a Bragg angle of 87.5°. The X-ray beam was focused to a FWHM of 5 µm and aligned to the centre of the optical beam.

The scattered photons were detected using three spherically bent Si(533) diced-crystal analysers positioned to cover scattering angles between 167° and 173°, with the Bragg reflection recorded by an Epix-100a detector. The system, including analysers and detector, was arranged on a 1-m-diameter Rowland circle. In addition, an Epix10k detector captured wide-angle X-ray scattering from 20° to 60°, enabling Laue diffraction analysis of the (111) and (200) planes of gold. During the experiment, we dynamically adjusted the timing between the optical heater and the X-ray probe from −1 ps to 6 ps, approximately the melt time of the sample, and utilized the MEC time tool to measure the on-shot delay between the X-ray and optical lasers[25].

The inherently low photon count per shot necessitates single-photon counting techniques, where each detected photon is converted to energy using the dispersion curve of the analysers. Multiple shots are then aggregated to construct a comprehensive spectral profile. The instrument function was determined by scattering from a room-temperature gold target, yielding the data in Fig. 2c. This spectrum was created from 7,486 photons accumulated over 749 shots. As the (422) diffraction peak of gold coincides with the analysers, the resulting spectrum predominantly reflects the elastic zero-phonon line, thus serving as a faithful representation of the instrument function. In this case, the resulting spectrum closely fits a Voigt profile, where the parameters γ and σ were determined using a maximum likelihood estimator and define the width of the Lorentzian and Gaussian components, respectively (see Methods for details). The FWHM of 44.7 meV is in agreement with previously measured widths[22,23] and is close to theoretical limits[24].

Laser heating of the target causes an increase in ion velocity, leading to Doppler broadening of the spectral lines, as seen by the red distribution in Fig. 2c. Unlike room-temperature experiments, the intense heating from each optical laser pulse destroys the target, necessitating a fresh gold sample for each measurement. This requirement slows the data collection process and, combined with time and target material constraints, limits the number of achievable shots. From our observations, approximately 300 detected photons from about 60 shots are sufficient to produce reasonable spectra and associated error estimates. The spectrum of heated gold, illustrated in Fig. 2c, shows considerable broadening. This broadening is quantitatively analysed using a maximum likelihood estimator, allowing for temperature calculations based on equation (1). Confidence intervals for the broadening, and thus the temperature estimates, are derived through rigorous bootstrapping (see Methods for details).

The result above represents a direct measurement of the ion temperature under high-temperature conditions at solid density, where only indirect methods have been used previously. The straightforward relationship between spectral broadening and temperature in equation (1) capitalizes on the large momentum transfer and elevated temperatures achieved through our backscattering geometry and extreme heating rates. These advancements have transformative potential for high-pressure and high-energy-density research, addressing a long-standing challenge in accurately determining temperature, which has often been a weak point in such studies[26–28]. In this work, we demonstrate its capability by investigating the ultimate stability limits of superheated materials.

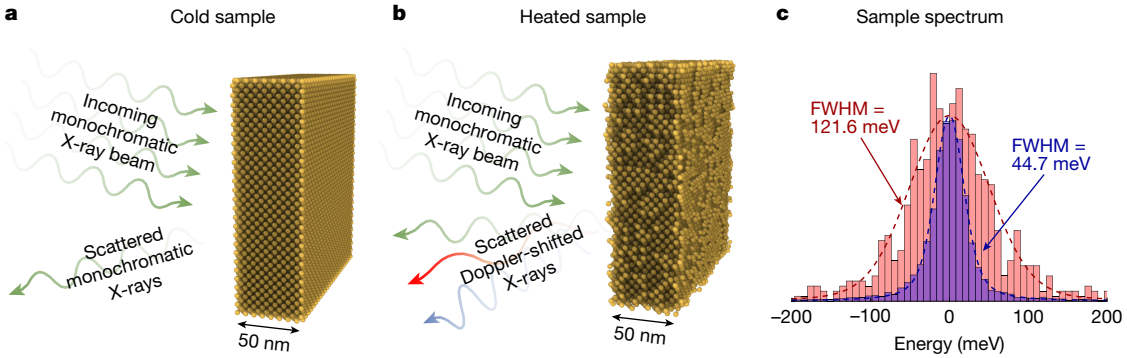

Fig. 2 | Illustration of method and example scattering spectra. a,**b**, An illustration of photon scattering from a cold sample (**a**) and a heated sample (**b**). Each X-ray pulse exposes the target to approximately 10^{10} photons at a central energy of E_0 = 7,491.9 eV within a narrow bandwidth ($\Delta E/E_0 = 4.3 \times 10^{-6}$). Approximately ten scattered photons are detected from each pulse. **c**, The energy distribution of scattered photons collected by the high-resolution X-ray spectrometer for a cold sample without a pump laser (purple, 7,486 photons) and a heated sample 3 ps after laser irradiation (red, 569 photons) at an incident optical fluence of 4.9 ± 0.5 J cm^{-2}. The distribution from the cold sample, representing the instrument function (IF) of the spectrometer, is well fitted by a Voigt profile with γ_{IF} = 9.5 meV and σ_{IF} = 14.2 meV, resulting in a FWHM of 44.7 meV. For the heated case, the distribution is also well fit by a Voigt profile with γ_{heated} = 9.5 meV and σ_{heated} = 47.2 meV, corresponding to a FWHM of 121.6 meV and an ion temperature of 19,000 K. Details of the fitting method can be found in Methods.

Lattice temperature evolution

We directly measured the ion temperature evolution in gold after laser irradiation by varying the delay between the optical pump and the X-ray probe. The optical pump generates ballistic electrons, which volumetrically heat the thermal electrons on a subpicosecond timescale[29]. Any inhomogeneities in electron heating are rapidly smoothed out by heat conduction of the thermal electrons, given their high thermal conductivity and subpicosecond diffusion timescale[30,31] (additional details in Methods). Rapid lattice heating occurs via electron–phonon energy transfer, with hot electrons serving as a thermal reservoir. The energy exchange rates are roughly proportional to the temperature difference, meaning that the energy transfer dynamics can be approximately controlled by the laser fluence. However, this information is not used in our analysis, as our approach allows for direct measurement of ion temperatures, bypassing the complexities of calculating electron–phonon energy exchange.

To allow us to accumulate multiple shots at the same conditions, we carefully measure all relevant experimental parameters—including on-target laser fluence, and the delay between the X-ray and optical pulses. On the basis of laser fluence, the data were divided into two categories, each representing a different heating rate. The lower-fluence scenario, depicted in Fig. 3a, encompasses fluences in the range of 1.9 ± 0.5 J cm^{-2}, resulting in a heating rate of approximately 3.5×10^{15} K s^{-1}; the higher-fluence scenario, shown in Fig. 3b, represents fluences in the range of 4.9 ± 0.5 J cm^{-2}, achieving a heating rate of approximately 6×10^{15} K s^{-1}.

The wide-angle X-ray detector, processed using the Dioptas software package[32], clearly displays the (111) and (200) Debye–Scherrer rings for time delays of up to 3 ps. The evolution of their azimuthally integrated diffraction intensities is included in Fig. 3. As the ions in the sample heat up, they vibrate increasingly around their equilibrium positions, reducing the intensity of these rings as predicted by Debye and Waller[33], with the (200) peak decaying faster than the (111) peak. Upon melting, the sample loses its long-range order, causing the Debye–Scherrer rings to disappear completely. We determine the time of melting from this visible loss of structure. At the heating rate of 3.5×10^{15} K s^{-1}, we are able

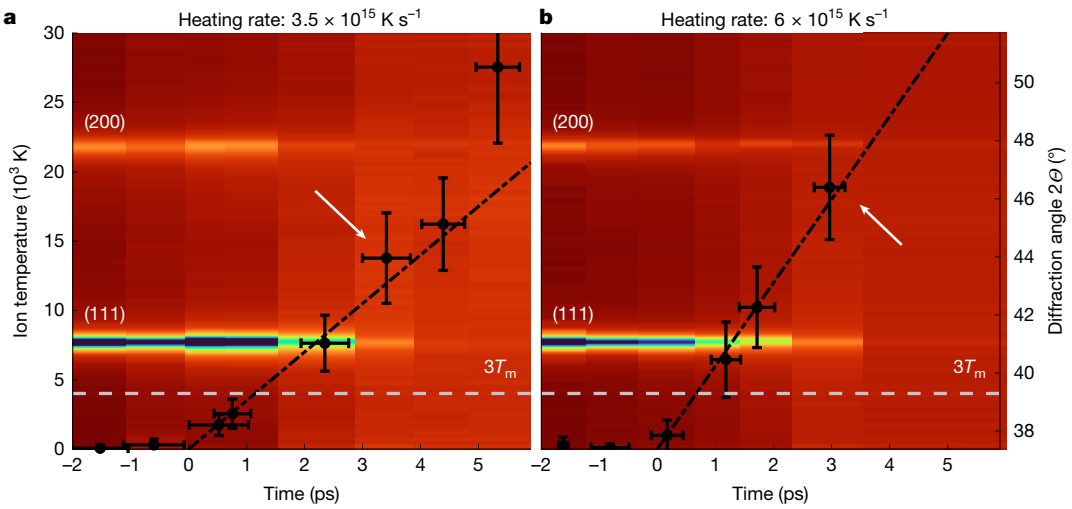

Fig. 3 | Ion temperature evolution. a,**b**, The measured ion temperature of a gold foil, shown by symbols with error bars, after irradiation with a laser fluence of 1.9 ± 0.5 J cm^{-2} (**a**) and 4.9 ± 0.5 J cm^{-2} (**b**). Error bars for the broadening are derived through a bootstrap resampling method (see Methods for details). These fluences result in heating rates of 3.5×10^{15} K s^{-1} and 6×10^{15} K s^{-1}, respectively (dashed line). Overlaid are the intensities of the (111) and (220) diffraction peaks whose disappearance can be used to identify the time of melting. Higher intensity is shown in blue. The white arrows indicate the highest temperature at which diffraction lines from a solid are observed. In both cases, the temperature of the superheated solid greatly exceeds the previously proposed limit of three times the melting temperature, shown by the horizontal dashed line.

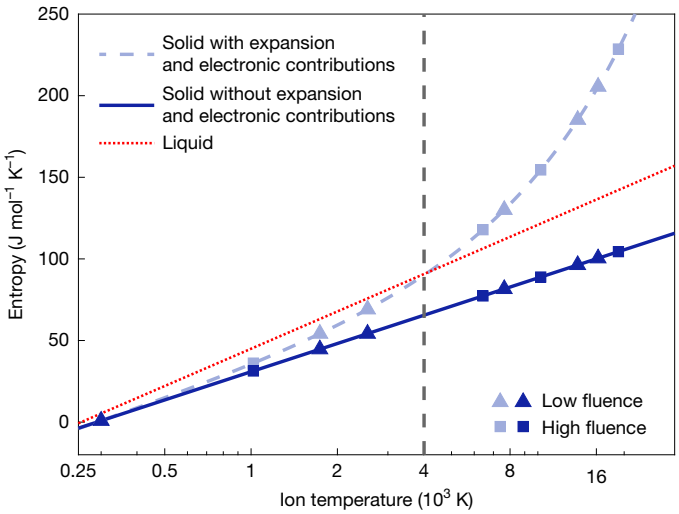

Fig. 4 | Calculated entropy for superheated gold. The calculated entropy is shown versus temperature for the solid (blue) and the liquid (red) phases. The results for the solids are calculated in two ways. The light-blue dashed curve shows the entropy including the terms for lattice expansion and changing electronic heat capacity. The dark-blue solid curve does not include these effects, corresponding to rapidly heated gold. For reference, the markers indicate the calculated entropy corresponding to the temperatures we measured in the solid material for the low-fluence (triangles) and high-fluence (squares) cases. The vertical dashed line denotes the originally proposed superheating limit[1]. Clearly, intense, ultrafast heating without sufficient time for lattice expansion can avoid the entropy catastrophe.

to heat the gold to a temperature of 13,800 ± 3,200 K, corresponding to about 10T_m. At the higher heating rate of 6×10^{15} K s^{-1}, samples were heated to a temperature of 19,000 ± 4,000 K, corresponding to about 14T_m. Notably, the temperatures exceed the proposed limit of 3T_m in both cases for over 2 ps. This time is approximately an order of magnitude longer than the characteristic phonon oscillation period[34] and, thus, much longer than required for homogeneous melting[35,36].

Discussion

The prediction of the entropy catastrophe is based on the thermodynamic principle that the entropy of a liquid cannot be lower than that of a solid with identical enthalpy[1,37,38]. Historically, the analysis of solid and liquid entropies identified two critical temperatures where extrapolated liquid entropy meets crystal entropy, beyond which thermodynamics is violated. The lower temperature, known as the Kauzmann temperature, necessitates a glass transition, triggering the sudden freezing into a crystalline phase[38–40]. The higher temperature, typically at 3T_m and termed the entropy catastrophe temperature, requires a sudden onset of melting. These temperatures delineate the proposed ultimate stability limits for superheating and supercooling.

Figure 4 illustrates the entropy profiles for the liquid and solid phases of gold, as originally proposed by Fecht and Johnson[1], who derived the entropy from the available heat capacities via

$$\Delta S = \int_{T_m}^{T} \frac{C_{\mathrm{liq/sol}}}{T'} \mathrm{d}T'. \quad (2)$$

The heat capacity of the liquid phase has been measured[41] as $C_{liq} = 32.97$ J mol^{-1} K^{-1}. For the solid, one finds $C_{sol} = 3R + \gamma T$, where the coefficient R refers to the gas constant and $\gamma = \gamma_{exp} + \gamma_{ele} = 6.6 \times 10^{-3}$ J mol^{-1} K^{-2} incorporates changes owing to the thermal expansion and heating of the electronic component, with expansion clearly dominating[41,42]: $\gamma_{exp} \approx 10\gamma_{ele}$. Again, the crossing point occurs at $T \approx 3T_m$, a limit we have surpassed by far.

The superheated states we have observed at temperatures far above the limit of the entropy catastrophe should not exist according to the calculation above (blue dashed line in Fig. 4). Indeed, if such a superheated system were to melt in isolation, it would undergo a spontaneous adiabatic process with a decrease in entropy, in direct violation of the second law of thermodynamics. To resolve this contradiction, we note that the crystal lattice does not undergo appreciable expansion or ablation within the timescales of our experiment. This fact is evident by the fixed location of the Bragg peak in Fig. 3 and is consistent with frequency-domain interferometry results observed in laser-excited gold[43,44] (additional details in Methods). Furthermore, the entropy associated with the electronic heat capacity, which already had only a minor role, remains approximately constant across the liquid and solid phases owing to the high electron temperature, which remains relatively stable. Thus, we find $\gamma_{ele} \approx 0$ and $\gamma_{exp} \approx 0$ for the situation created in our experiment. Applying these approximations in equation (2), we obtain the solid-blue line in Fig. 4. This entropy for the solid remains below the liquid entropy for all temperatures, allowing us to surpass the previously proposed limit as long as the heating occurs fast enough to preclude expansion. In essence, the crossing of the two entropy curves is effectively eliminated by ultrafast intense heating, indicating that superheating may not have an upper bound.

Our experimental findings raise an important question about the ultimate stability limit for superheating. In the regime explored, the heat capacity of the solid is governed by universal constants, and its general form remains insufficiently characterized for the liquid[45]. Therefore, it is unknown whether the entropies of solids and liquids cross at higher temperatures. Moreover, heat capacity variations in non-equilibrium systems and thin films could further alter the entropy balance. Consequently, it is uncertain whether arguments based on the crossing point of entropy curves, similar to the lower-temperature Kauzmann limit, apply here. Nevertheless, our experiments clearly demonstrate that the previously proposed limit of superheating can be exceeded by far if the material is heated fast enough.

Online content

Any methods, additional references, Nature Portfolio reporting summaries, source data, extended data, supplementary information, acknowledgements, peer review information; details of author contributions and competing interests; and statements of data and code availability are available at https://doi.org/10.1038/s41586-025-09253-y.

1. Fecht, J. & Johnson, W. L. Entropy and enthalpy catastrophe as a stability limit for crystalline material. *Nature* **334**, 50–51 (1988).
2. Lele, S., Rao, P. R. & Dubey, K. S. Entropy catastrophe and superheating of crystals. *Nature* **336**, 567–568 (1988).
3. Tallon, J. L. A hierarchy of catastrophes as a succession of stability limits for the crystalline state. *Nature* **342**, 658–660 (1989).
4. Lu, K. & Li, Y. Homogeneous nucleation catastrophe as a kinetic stability limit for superheated crystal. *Phys. Rev. Lett.* **80**, 4474–4477 (1998).
5. Luo, S.-N. & Ahrens, T. J. Superheating systematics of crystalline solids. *Appl. Phys. Lett.* **82**, 1836–1838 (2003).
6. Gamaly, E. G. Ultra-fast disordering by fs-lasers: lattice superheating prior to the entropy catastrophe. *Appl. Phys. A* **101**, 205–208 (2010).
7. Seok Hwang, Y. & Levitas, V. I. Phase field simulation of kinetic superheating and melting of aluminum nanolayer irradiated by pico- and femtosecond laser. *Appl. Phys. Lett.* **103**, 263107 (2013).
8. Siwick, B. J., Dwyer, J. R., Jordan, R. E. & Miller, R. J. D. An atomic-level view of melting using femtosecond electron diffraction. *Science* **302**, 1382–1385 (2003).
9. Williamson, S., Mourou, G. & Li, J. C. M. Time-resolved laser-induced phase transformation in aluminum. *Phys. Rev. Lett.* **52**, 2364–2367 (1984).
10. Dwyer, J. R. et al. Femtosecond electron diffraction: an atomic perspective of condensed phase dynamics. *J. Mod. Opt.* **54**, 905–922 (2007).
11. Ernstorfer, R. et al. The formation of warm dense matter: experimental evidence for electronic bond hardening in gold. *Science* **323**, 1033–1037 (2009).
12. Molina, J. M. & White, T. G. A molecular dynamics study of laser-excited gold. *Matter Radiat. Extremes* **7**, 036901 (2022).

13. Bosak, A. & Krisch, M. Phonon density of states probed by inelastic X-ray scattering. *Phys. Rev. B* **72**, 224305 (2005).
14. Baron, A. Q. in *Synchrotron Light Sources and Free-Electron Lasers: Accelerator Physics, Instrumentation and Science Applications* (eds Jaeschke, E. J. et al.) 1643–1719 (Springer, 2016).
15. Rüffer, R. & Chumakov, A. I. in *Synchrotron Light Sources and Free-Electron Lasers: Accelerator Physics, Instrumentation and Science Applications* (eds Jaeschke, E. J. et al.) 2251–2287 (Springer, 2020).
16. Ritzmann, U., Oppeneer, P. M. & Maldonado, P. Theory of out-of-equilibrium electron and phonon dynamics in metals after femtosecond laser excitation. *Phys. Rev. B* **102**, 214305 (2020).
17. Drake, G. W. F. (ed.) *Springer Handbook of Atomic, Molecular, and Optical Physics. Springer Handbooks* (Springer, 2023).
18. Monaco, G., Cunsolo, A., Pratesi, G., Sette, F. & Verbeni, R. Deep inelastic atomic scattering of X rays in liquid neon. *Phys. Rev. Lett.* **88**, 227401 (2002).
19. Nagler, B. et al. The matter in extreme conditions instrument at the linac coherent light source. *J. Synchrotron Radiat.* **22**, 520–525 (2015).
20. Glenzer, S. H. et al. Matter under extreme conditions experiments at the Linac Coherent Light Source. *J. Phys. B* **49**, 092001 (2016).
21. Verbeni, R. et al. Advances in crystal analyzers for inelastic X-ray scattering. *J. Phys. Chem. Solids* **66**, 2299–2305 (2005).
22. McBride, E. E. et al. Setup for meV-resolution inelastic X-ray scattering measurements and X-ray diffraction at the Matter in Extreme Conditions endstation at the Linac Coherent Light Source. *Rev. Sci. Instrum.* **89**, 10F104 (2018).
23. White, T. G. et al. Speed of sound in methane under conditions of planetary interiors. *Phys. Rev. Res.* **6**, L022029 (2024).
24. Wollenweber, L. et al. High-resolution inelastic X-ray scattering at the high energy density scientific instrument at the European X-Ray Free-Electron Laser. *Rev. Sci. Instrum.* **92**, 013101 (2021).
25. Descamps, A. et al. Evidence for phonon hardening in laser-excited gold using X-ray diffraction at a hard X-ray free electron laser. *Sci. Adv.* **10**, eadh5272 (2024).
26. Kraus, R. G. et al. Measuring the melting curve of iron at super-Earth core conditions. *Science* **375**, 202–205 (2022).
27. Dornheim, T. et al. Accurate temperature diagnostics for matter under extreme conditions. *Nat. Commun.* **13**, 7911 (2022).
28. Benedetti, L. R. et al. Dissociation of CH_4 at high pressures and temperatures: diamond formation in giant planet interiors? *Science* **286**, 100–102 (1999).
29. Chen, Z. et al. Evolution of ac conductivity in nonequilibrium warm dense gold. *Phys. Rev. Lett.* **110**, 135001 (2013).
30. Petrov, Y. V., Inogamov, N. A. & Migdal, K. P. Thermal conductivity and the electron-ion heat transfer coefficient in condensed media with a strongly excited electron subsystem. *JETP Lett.* **97**, 20–27 (2013).
31. Petrov, Y. V., Migdal, K. P., Inogamov, N. A. & Zhakhovsky, V. V. Two-temperature equation of state for aluminum and gold with electrons excited by an ultrashort laser pulse. *Appl. Phys. B* **119**, 401–411 (2015).
32. Prescher, C. & Prakapenka, V. B. DIOPTAS: a program for reduction of two-dimensional X-ray diffraction data and data exploration. *High Pressure Res.* **35**, 223–230 (2015).
33. Warren, B. E. *X-ray Diffraction* (Dover, 1990).
34. Lynn, J. W., Smith, H. G. & Nicklow, R. M. Lattice dynamics of gold. *Phys. Rev. B* **8**, 3493–3499 (1973).
35. Mo, M. Z. et al. Heterogeneous to homogeneous melting transition visualized with ultrafast electron diffraction. *Science* **360**, 1451–1455 (2018).
36. Rethfeld, B., Sokolowski-Tinten, K., von der Linde, D. & Anisimov, S. I. Ultrafast thermal melting of laser-excited solids by homogeneous nucleation. *Phys. Rev. B* **65**, 092103 (2002).
37. Speedy, R. J. Kauzmann's paradox and the glass transition. *Biophys. Chem.* **105**, 411–420 (2003).
38. Kauzmann, W. The nature of the glassy state and the behavior of liquids at low temperatures. *Chem. Rev.* **43**, 219–256 (1948).
39. Berthier, L. & Reichman, D. R. Modern computational studies of the glass transition. *Nat. Rev. Phys.* **5**, 102–116 (2023).
40. Welch, R. S. et al. Cracking the Kauzmann paradox. *Acta Mater.* **254**, 118994 (2023).
41. Arblaster, J. W. Thermodynamic properties of gold. *J. Phase Equilibria Diffus.* **37**, 229–245 (2016).
42. Lin, Z., Zhigilei, L. V. & Celli, V. Electron–phonon coupling and electron heat capacity of metals under conditions of strong electron–phonon nonequilibrium. *Phys. Rev. B* **77**, 075133 (2008).
43. Chen, Z. et al. Interatomic potential in the nonequilibrium warm dense matter regime. *Phys. Rev. Lett.* **121**, 075002 (2018).
44. Ao, T. et al. Optical properties in nonequilibrium phase transitions. *Phys. Rev. Lett.* **96**, 055001 (2006).
45. Baggioli, M. & Zaccone, A. Explaining the specific heat of liquids based on instantaneous normal modes. *Phys. Rev. E* **104**, 014103 (2021).

Methods

Maximum likelihood estimator

The energy distribution of scattered photons is well described by a Voigt function $V_{\gamma,\sigma}(E)$, which is the convolution of a Gaussian distribution with standard deviation σ and a Lorentzian (Cauchy) distribution with width parameter γ. In this study, we determined all Voigt profiles using a maximum likelihood estimator. Specifically, we maximized the log-likelihood function for the parameters σ and γ, given the observed photon energies $\{E_i\}$, where $i = 1, 2, \ldots, N$ and N is the number of detected photons:

$$\log\mathcal{L}(\gamma,\sigma) = \sum_{i=1}^{N} \log[V_{\gamma,\sigma}(E_i)].$$

For practical application, we employed the maximum likelihood estimator to estimate the σ value of the Voigt profile from the experimental data while keeping γ fixed to the value determined for the instrument function (that is, the known broadening due to the instrument). The thermal broadening $\Delta E_{\mathrm{therm}}$ can then be found from the refined σ_{heated} value and the instrument function σ_{IF} (the standard deviation of the Gaussian component for the cold sample) using:

$$\Delta E_{\mathrm{therm}} = 2\sqrt{2\ln 2}\sqrt{\sigma_{\mathrm{heated}}{}^2 - \sigma_{\mathrm{IF}}{}^2}.$$

An example of this application is shown in Fig. 2c, where the experimental data (appropriately binned) are well fitted by the Voigt function with parameters estimated via the maximum likelihood estimator. To assess the reliability of these parameters, we applied bootstrapping methods to generate confidence intervals. By randomly drawing N samples from the observed distribution of photon energies $\{E_i\}$, we recalculated the parameters over approximately 1,000 iterations. This process allowed us to construct a distribution for σ, from which we derived the bias and confidence intervals of the estimator. Our analysis confirms that the bias is minimal relative to the width of the confidence intervals for the typical sample size of $N \approx 300$ measured photons, and we corrected the results for any detected bias. The 1σ confidence intervals for these measurements are illustrated in Fig. 3.

Applicability of the broadening–temperature relation

Equation (1) in the main text remains applicable in this regime because we are effectively sampling a sufficiently large number of independent scattering events. At large wavenumber Q, the measurement probes individual interactions, and by the central limit theorem, the resulting distribution of energy transfers leads to a well-defined spectral width that is independent of the underlying microscopic details. To model the scattering process more rigorously, we employ a multiphonon expansion[14]. In this approach, the scattering is treated as a Poisson distribution over multiphonon events, where the contribution from scattering by n phonons is constructed via n convolutions of the single-phonon scattering spectrum, as described in several sources[15]. Specifically, in our implementation, we approximate the single-phonon scattering spectrum at large Q as $g(E)/E^2$, where $g(E)$ is the generalized phonon density of states applicable in this regime[13]. As shown in Extended Data Fig. 1, we compare both approaches and find excellent agreement above 2,000 K, reinforcing the validity of equation (1) in this regime. This consistency further supports the simpler formulation used in the main text while ensuring that the key physical effects are accurately captured.

Heating uniformity in 50-nm gold

Understanding the uniformity of electron heating is crucial for our analysis. Here we provide details supporting the assumption of uniform heating within our 50 nm gold samples. The primary factor is the penetration depth of the ballistic electrons used to heat the target, which has been measured to be approximately 100 nm (ref. 29). This ensures that our 50-nm sample is homogeneously heated. In addition, any residual inhomogeneities left by the ballistic electrons will be rapidly smoothed out by heat conduction from thermal electrons, further ensuring a uniform temperature distribution. The electron thermal conductivity at these conditions is between[30] 3,000 W K^{-1} m^{-1} and 5,000 W K^{-1} m^{-1}, and the electron heat capacity is approximately[31] 0.3–0.5 J g^{-1} K^{-1}. From these values, we estimate the thermal diffusion time across the 50-nm sample to be on the order of 0.5 ps. Finally, as additional evidence, we note that previous studies in which gold was heated to energy densities comparable to our lowest-fluence case observed similar expansion and dissociation dynamics in 35-nm films[44]. This agreement suggests that our slightly thicker targets experience comparable heating conditions and are unlikely to exhibit appreciable temperature gradients.

Wide-angle X-ray detector calibration

All X-ray diffraction patterns were processed using the Dioptas software package. For calibration, polycrystalline LaB6 was used to establish the relationship between pixel positions on the detector and the corresponding scattering angles, as illustrated in Extended Data Fig. 2. To correct for variations among the detector pixels, we subtracted a dark-field image from the dataset. In addition, we corrected for the varying solid angle coverage of each pixel relative to the scattering target. Transmission corrections were applied to account for attenuation due to the layers of 50-µm aluminium and 125-µm polyimide present in the beam path. The data processing also incorporated a polarization correction factor, $P(\theta, \phi) = 1 - \sin(2\theta)\cos(2\phi)$, where θ is the scattering angle and ϕ is the angle between the plane of the scattering vector and the polarization direction of the incoming X-rays.

Optical laser fluence

To vary the laser fluence in the experiment, we used an iris before the final focusing optics, enabling control over the two laser fluence levels discussed in this work. We calculated the absolute laser fluence for each shot, allowing us to include only the scattered X-ray photons corresponding to specific fluence bands in our analysis. We first measured the laser energy for each shot and accounted for spatial jitter using a calibrated equivalent plane camera. The laser intensity profile was determined by combining these measurements with images of the laser spot taken in the focal plane, as shown in Extended Data Fig. 3. Knowing the precise location of the X-ray beam relative to the laser spot allowed us to calculate the fluence at the point of X-ray interaction for each shot. The X-ray beam position was periodically updated using a yttrium-aluminium-garnet crystal screen, which provided the pixel location of the X-ray beam on the detector. This calibration ensured accurate alignment between the laser spot and the X-ray probe, allowing precise calculation of the laser fluence at the interaction point.

Inelastic X-ray scattering spectrometer dispersion calculation

The diffraction from the (533) plane of each of the three high-resolution silicon diced-crystal analysers was found to lie along an arc with a radius of 1,745.5 pixels (87.3 mm) on the detector (Extended Data Fig. 4). Considering a pixel size of 50 µm, we determined the incident X-ray energy to be 7,491.9 eV and calculated an energy dispersion of 8.187 meV per pixel, or equivalently, 0.164 meV per µm.

Determination of target density

In this work, the diffraction of the Bragg peaks was collected simultaneously with the temperature measurements, enabling experimental determination of the melting point and target expansion. Extended Data Fig. 5a,b illustrates the decay of the (111) Bragg peak for the two fluence cases examined in this study. The decay of the Bragg peak over time reflects the increased thermal motion of atoms around their lattice sites. For both cases, the last solid time delay, as discussed in the main text, was defined by the final delay at which the (111) Bragg peak remained visible, specifically at 3.4 ps and 2.95 ps for the low- and

high-fluence cases, respectively. In addition, Extended Data Fig. 5c,d highlights the variation in the position of the peak centre over time. The absence of a shift in the peak centre with time delay indicates that the target density remains constant up to the melting point.

Data availability

The data that support the findings of this study are available on Zenodo (https://doi.org/10.5281/zenodo.15445637)[46].

46. White, T. G. et al. Superheating gold beyond the predicted entropy catastrophe threshold data. *Zenodo* https://doi.org/10.5281/zenodo.15445637 (2025).

Acknowledgements T.G.W. thanks Y. Barlas for discussions. The work of T.G.W. was supported in part by the US Department of Energy, National Nuclear Security Administration under award number DE-NA0004039. This material is based upon work supported by the US Department of Energy, Office of Science, Office of Fusion Energy Sciences under award number DE-SC0019268. T.G.W. also acknowledges support from the Clemons-Magee Endowed Professorship in Physics at the University of Nevada, Reno. This work was also supported by the UK Research and Innovation Future Leaders Fellowship (MR/W008211/1) awarded to E.E.M. The work of S.H.G. was supported by the US Department of Energy, Office of Science, Fusion Energy Sciences under FWP numbers 100182 and 100866, and by the National Science Foundation under grant numbers 1632708 and PHY-2308860. G.M. acknowledges support from the GLAXES project, ERC-2021-ADG (grant agreement number 101053167), funded by the European Union. The work of L.B.F. was supported by the US Department of Energy, Office of Science, Fusion Energy Sciences under FWP 100866, and by the Department of Energy Laboratory Directed Research and Development (LDRD) programme at SLAC National Accelerator Laboratory under contract number DE-AC02-76SF00515. Use of the Linac Coherent Light Source (LCLS) at SLAC National Accelerator Laboratory is supported by the US Department of Energy, Office of Science, Office of Basic Energy Sciences under contract number DE-AC02-76SF00515. The MEC instrument is supported by the US Department of Energy, Office of Science, Office of Fusion Energy Sciences under the same contract.

Author contributions T.G.W. and B.N. conceived of the project, led the experiment and wrote the paper. T.D.G., D.H., J.I., L.M. and D.O.G. performed the data analysis. D.H., H.J.L., E.G., E.C., D.K., A.D., B.A., L.W., E.E.M., C.C. and S.Y. participated in the experiment. S.Y. and E.G. also operated and analysed the time tool diagnostic. S.H.G., G.G., K.A., S.G., G.M., U.Z., J.B.H. and L.B.F. provided expertise on high-resolution X-ray scattering and free electron laser instrumentation. J.M. contributed to early exploratory work that helped inspire the present study, and S.H.G. further helped develop its motivation. D.O.G. and H.S. assisted with post-experiment theory development. All authors provided feedback and editorial input on the paper.

Competing interests The authors declare no competing interests.

Additional information
Correspondence and requests for materials should be addressed to Thomas G. White.
Peer review information *Nature* thanks Yasuhiko Sentoku, Artur Tamm and the other, anonymous, reviewer(s) for their contribution to the peer review of this work.

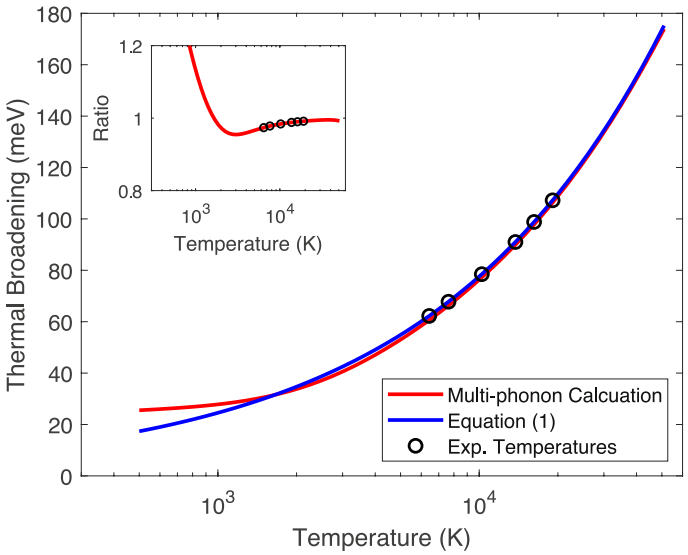

Extended Data Fig. 1 | Thermal broadening comparison. Comparison of thermal broadening predicted by the multi-phonon scattering calculation (red) and Eq. (1) (blue). The two approaches show excellent agreement above 2000 K, supporting the use of the simpler formulation at high temperatures. The inset shows the ratio of the two methods, demonstrating convergence in this regime. The circles represent temperatures measured in this work that exceed the originally proposed entropy catastrophe threshold ($3T_m$). The difference between the two approaches for the highest temperatures is less than 1%.

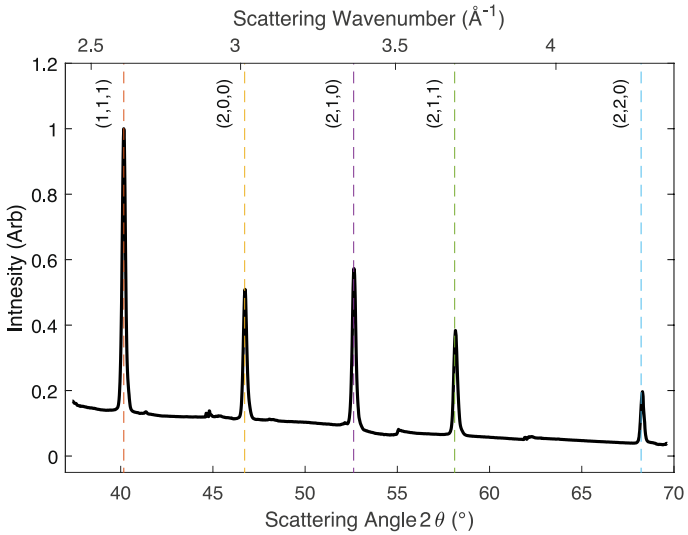

Extended Data Fig. 2 | Diffraction peak intensity for LaB_6. X-ray diffraction peaks were obtained from polycrystalline LaB_6 using an X-ray energy of 7491.9 eV. The diffraction pattern was processed using the Dioptas software, and the integrated intensity is plotted as a function of scattering angle (in degrees) and scattering vector q (in Å^{-1}). The detector was calibrated by aligning the observed diffraction peaks with the predicted positions of the first five LaB_6 diffraction lines, indicated by dashed lines.

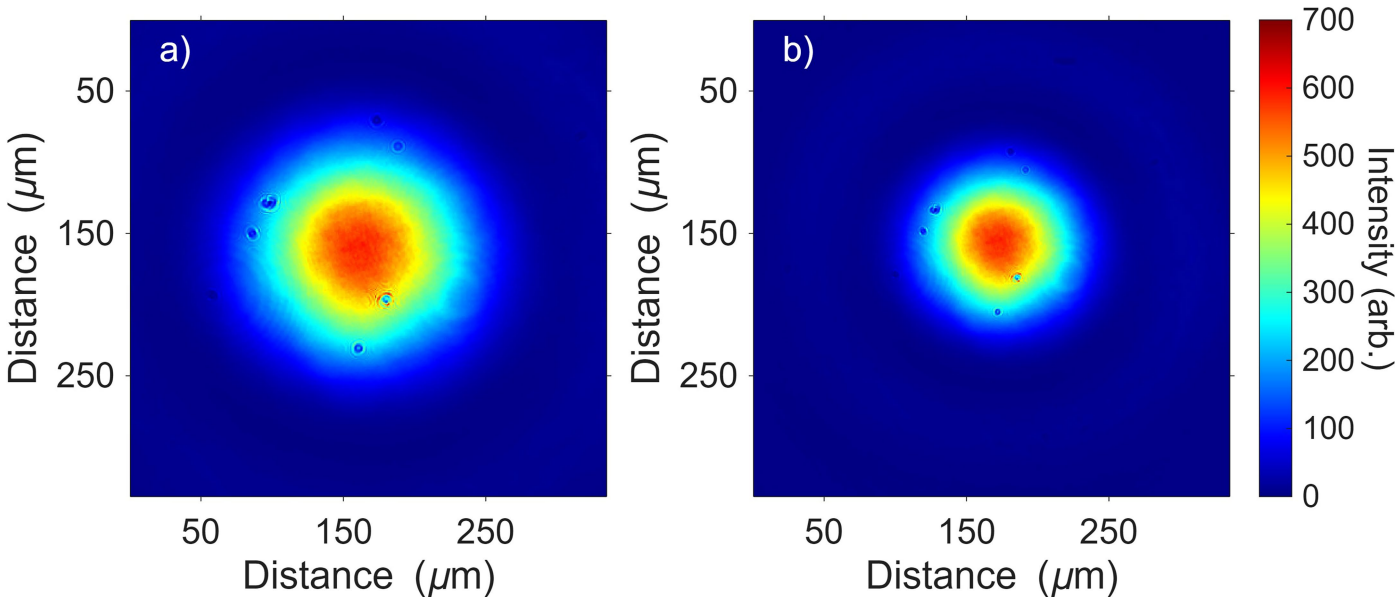

Extended Data Fig. 3 | Optical laser spot images. Images of the optical laser spots captured at the focal plane for the **a**, low fluence (1.9 ± 0.5 J/cm^2) and **b**, high fluence (4.9 ± 0.5 J/cm^2) cases. For the low fluence case, the laser spot has a FWHM of approximately 150 µm, while for the high fluence case, the FWHM is approximately 100 µm.

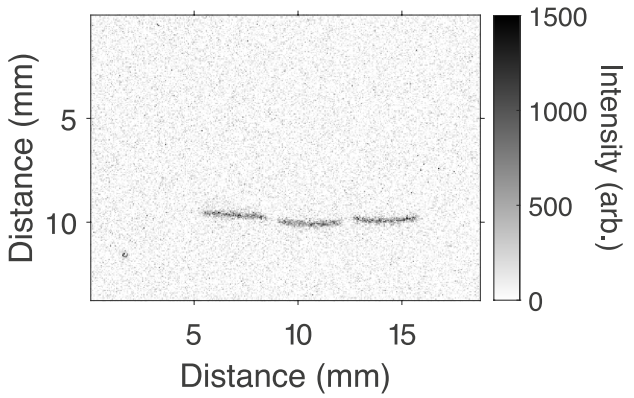

Extended Data Fig. 4 | Inelastic X-ray scattering detector. The signal from an undriven 50 nm gold foil was detected by three (533) silicon diced-crystal analysers. The precise X-ray energy of the probe and the resulting energy dispersion are accurately determined from the positions of the three arcs.

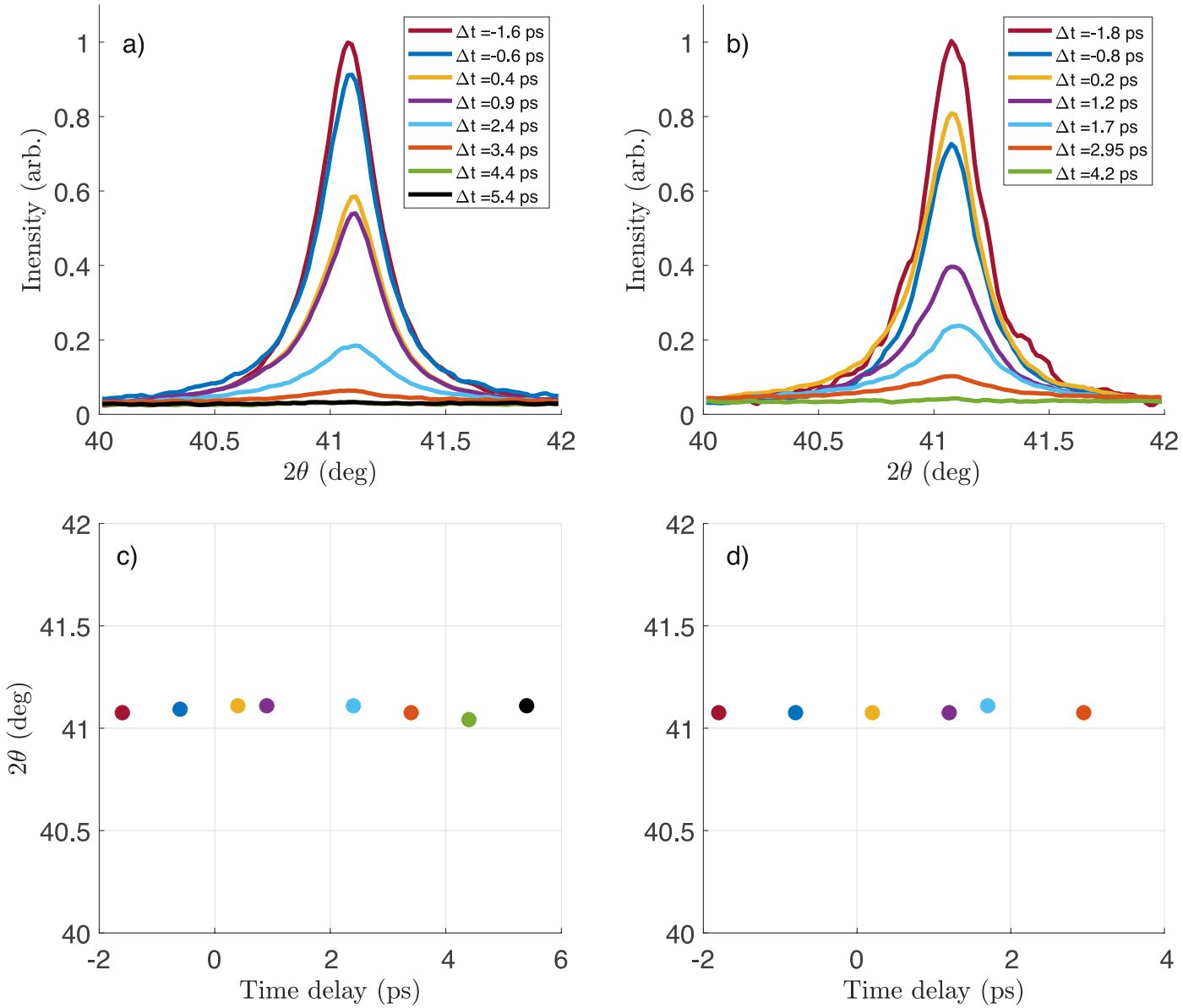

Extended Data Fig. 5 | Evolution of the gold (111) diffraction peak. X-ray diffraction of the (111) Bragg peak for the two laser fluence cases discussed in this work. **a**,**b**, Decay of the (111) Bragg peak for the low and high fluence cases, respectively, at various time delays. The progressive decay of the peak reflects the increasing thermal motion of atoms. **c**,**d**, Centre position of the (111) peak for the low and high fluence cases, respectively. In both cases, the absence of a shift in peak position over time indicates a constant target density up to the melting point.